Development of slow-burning solid rocket booster for RLV-TD hypersonic experiment

Achutananda Parhi*, V. Mahesh, Khadarvoli Kalluru, S. Reshmi, R. Harikrishnan, V. M. Lakshmi, J. Paul Murugan and Renjith Kumar Reddy

Vikram Sarabhai Space Centre, Indian Space Research Organisation, Thiruvananthapuram 695 022, India

This article discusses the developmental challenges of the low-thrust, long-duration solid rocket motor for the launch of the experimental Reusable Launch Vehicle-Technological Demonstrator (RLV-TD). The main challenges were: (1) developing a motor case and subsystems with low inert mass; (2) design of an optimum nozzle such that the motor can have maximum specific impulse at atmospheric conditions, but with no flow separation at low operation pressures; (3) developing a slow-burning propellant (3 mm/s) to meet the mission requirements; (4) design of propellant grain for the motor so that it has long burning time, the vehicle experiences low dynamic pressure at the transonic regime, and the motor is without combustion instability; (5) developing necessary thermal protection system to take care of long-duration operations, and (6) developing the igniter to ensure the ignition of the motor, especially when easy ignition is difficult with slow-burning propellants and that there should be sufficient overlap of igniter functioning with motor initiation. Performance of the motor in flight indicated that the design met all the required criteria within the expected tolerance.

Keywords: Burning rate, igniter, motor case, performance prediction, solid rocket booster.

Introduction

REUSABLE Launch Vehicle-Technology Demonstrator-Hypersonic Experiment-01 (RLV-TD-HEX-01) was intended to demonstrate the operational capability of a winged body vehicle (RLV) to orbit and return to the earth for re-use. In the HEX-01 mission, the RLV-TD is lifted to the required altitude of 30–35 km and Mach number of ~5 by a 1 m diameter solid booster (HS9) carrying about 9 tonnes of solid propellant. The mission analysis indicated that the motor should have an action time of ~90 s with a thrust level of ~250 kN. An important requirement for the motor is to shape the propulsive thrust such that the peak dynamic pressure at transonic region is at a permissible level. The requirement of long action time for the motor necessitates developing a slow-burning propellant. The nozzle throat material was composite carbon phenolic. The thrust vector controlling was done by secondary injection thrust vector control (SITVC) at the nozzle divergent. The first static test of this motor was successfully carried out at the Satish Dhawan Space Centre (SDSC), Sriharikota on 19 November 2008; the motor performed satisfactorily, as expected. However, based on the detailed post-test assessment and the revised mission requirements, certain modifications were incorporated in the propellant grain configuration to tailor the maximum dynamic pressure acting on the vehicle. Also, the igniter design was modified to have sufficient overlap of igniter functioning with the motor pressure rise. With these modifications, the second static test was successfully conducted on 3 August 2011 and the motor was inducted to RLV-TD-HEX-01 flight. RLV-TD-HEX-01 launch was accomplished on 23 May 2016.

*For correspondence. (e-mail: achutananda_parhi@vssc.gov.in)

Design of the HS9 booster

The RLV-TD-HEX-01 mission profile indicated that the HS9 booster was active up to an altitude of 30–35 km; later, it separated from the RLV and fell into the Bay of Bengal. Based on mission optimization studies, the specifications for the mission profile have been arrived (Table 1). Ideal thrust profile was used by the motor design team to develop the HS9 booster (Figure 1). The required ballistic performance parameters for the HS9 booster were arrived at from the ideal thrust profile with expected dispersion in the performance parameters (Table 2). In addition, the outer diameter of the motor was fixed as 1 m. Initial design assessments revealed that, slow-burning propellant with a burn rate of 3 mm/s needs to be developed and qualified, as the readily available formulation failed to meet the mission requirements. Figure 1 provides a comparison of mission requirements graph with those of other strap-on motors.

Propellant development

The real challenge for the grain design was to achieve an action time of ~90 s within the diameter constraint of 1 m of the motor along with meeting the prescribed thrust–time

profile. The qualified slowest burning rate propellant available had a burning rate of ~5 mm/s, which would give a motor action time of ~50 s only (Figure 1). This propellant formulation contains hydroxyl terminated polybutadiene as binder, ammonium per chlorate (AP) as oxidizer and aluminum powder as fuel without burning rate catalyst. In fact, the propellant contains coarse AP particles at the highest proportion (4 : 1) against the fine AP particles. The burning rate could be further reduced by increasing the coarse fraction, but it severely affects the casting ability of the propellant and mechanical properties. Hence it was decided to reduce the burning rate using a burning rate retardant. A large number of burning rate retardants such as ammonium sulphate, di-ammonium hydrogen phosphate, ammonium oxalate, lithium fluoride, calcium carbonate and oxamide were considered[1]. Among these, oxamide was finally selected based on its effectiveness in bringing down the burning rate and maintaining the mechanical properties close to those of the parent composition propellant (Table 3). During combustion of the propellant, AP decomposes to form lower molecular weight fragments, including ammonia[2]. The oxamide also decomposes in the same temperature regime, liberating ammonia and retarding the decomposing process of AP and moderating the burning rate characteristics of the propellant[2]. Extensive ageing studies at higher temperature (60°C) for 180 days and at room temperature (30–32°C) for 1200 days proved that the mechanical properties of the propellant are retained during storage, similar to the parent propellant. However, comparatively higher concentration of oxamide (~3%) is required to bring down the burning rate to the required level. This brought down the specific impulse by 3 s compared to its parent uncatalysed propellant. In addition, the propellant exhibited slightly higher ignition delay. The total solid loading (AP + Al + oxamide) of the finalized formulation was 85%.

Table 1. Mission specifications of the solid booster for Reusable Launch Vehicle (RLV)

Parameter	Specification
Mach number at motor burn out	>6
Dynamic pressure (kPa)	≤34
q_α (Pa.radian)	≤180
Flight path angle at burn out (deg)	<25

q_α, Aerodynamic load indicator.

Table 2. Performance requirements of the solid booster for RLV

Parameter	Preliminary design specifications
Propellant mass (kg)	~9200 ± 50
Action time (s)	~90 ± 3
Maximum thrust (kN)	~320
Maximum allowable pressure (MPa)	<2.55
Total impulse (Mega Newton-s)	~23.6

Motor grain design and thrust shaping

In order to meet the requirements given in Table 2, a large number of grain configurations were considered during the developmental phase of the motor (Figure 2). For all the options, a three-segmented configuration was chosen based on the casting capability of the plant. For

Table 3. Comparison of typical mechanical properties of the slow-burning propellants with the parent propellant

Parameter	Parent propellant	Slow burning propellant
Tensile strength (kg/cm^2)	8.0	8.5
% Elongation	40	48
Modulus (kg/cm^2)	50	45
Hardness (Shore A)	70	70
Density (kg/m^3)	1760	1750
Slurry viscosity (Pa.s)	520–650	500–650

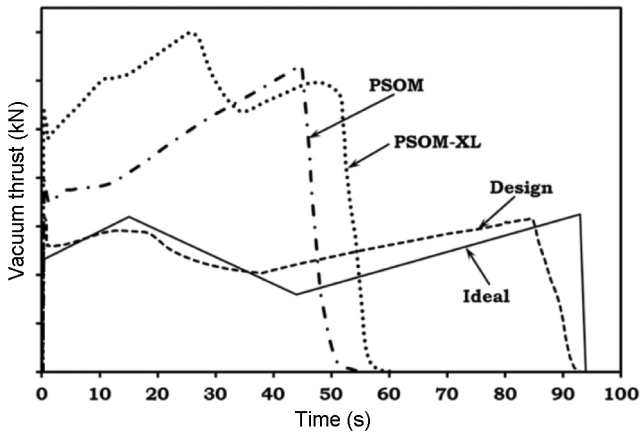

Figure 1. Comparison of the HS9 motor thrust–time profile (designed) with thrust profiles of other 1 m diameter class motors.

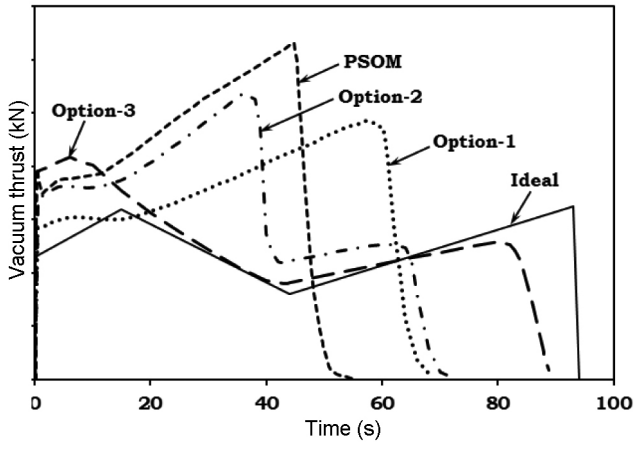

Figure 2. Performance of various options considered for the HS9 motor.

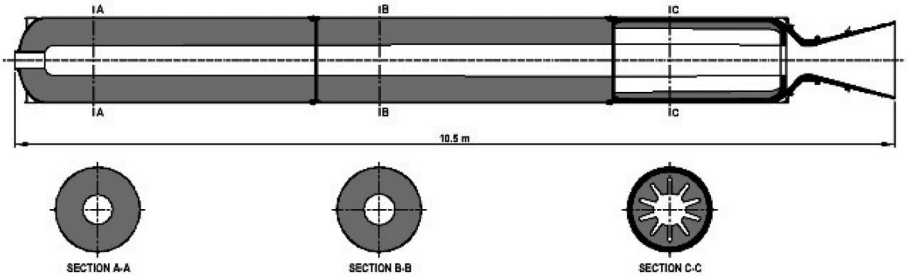

Figure 3. Finalized grain configuration of the HS9 motor for RLV-TD.

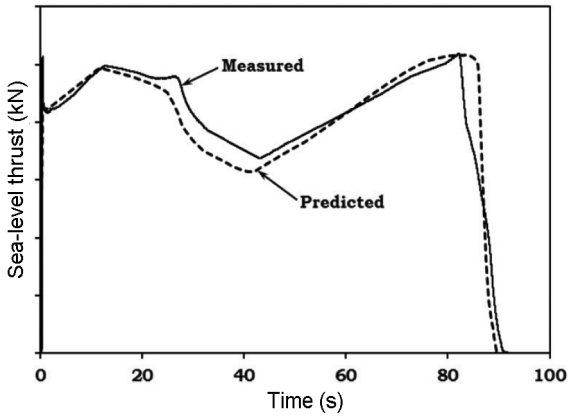

Figure 4. Comparison of the predicted and measured thrust–time histories of RLV-ST01 motor.

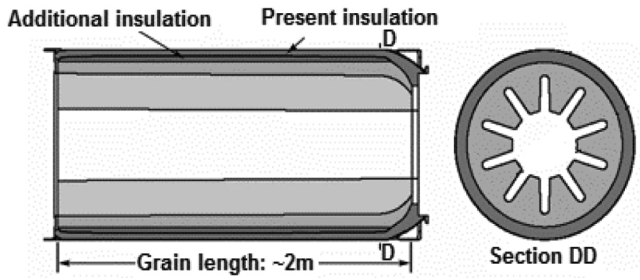

Figure 5. Modification made on the nozzle-end segment.

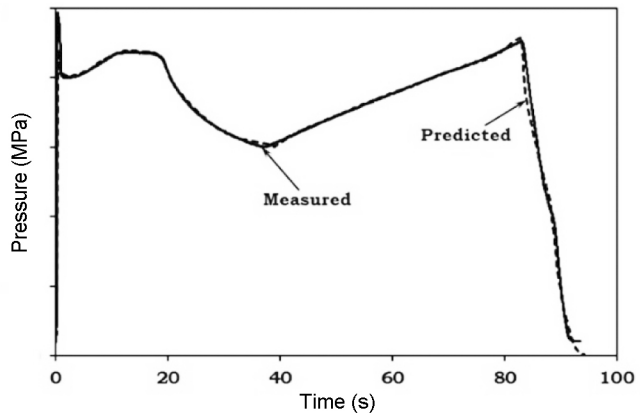

Figure 6. Comparison of the predicted and measured pressure–time histories of the RLV-ST02 motor.

the head-end segment, eight-lobes deep-slotted star configuration and, for the middle and nozzle-end segments cylindrical port configurations were adopted. The combination of normal, fast and slow-burning propellants was considered for different segments. It was observed that all slow-burning propellant options gave approximately similar thrust profiles as required by the mission. However, the possibility of higher erosive burning was found with this configuration and finally the star configuration at head-end was shifted to the nozzle-end to reduce the high cross-flow velocity effect. Figure 3 shows the finalized grain configuration of the HS9 motor. Predicted and measured thrust–time histories of RLV-ST-01 motor are given in Figure 4. The head-end and middle segments were provided with cylindrical ports, while the nozzle-end segment was provided with a deep-slotted star port configuration as shown in Figure 5. This will increase the initial burning surface area so that the initial thrust of the motor was sufficiently high. Total motor length was ~10 m. The propellant mass of the head-end and middle segments was about 4 tonnes each, while the propellant mass of the nozzle-end segment was 1.2 tonnes. With the modification of the grain profile, initial thrust requirements were met. The volumetric loading was ~80%. Predicted and measured pressure–time histories of the RLV-ST02 motor are shown in Figure 6.

Nozzle design

Conical convergent–divergent-type nozzle was for this motor not only due to the inherent simplicity in fabrication, but also for the application of SITVC. An area ratio of 7 was chosen because the motor was to be operated in lower atmospheric regime (~35 km) and nozzle flow separation was to be avoided[3,4]. However, in static test, nozzle flow separation occurred for a duration of ~15 s when the motor was operated at lowest operating chamber pressure (at ~40 s). However, in actual flight such flow separation will not be experienced because the rocket will be at a higher altitude during the flight regime. This was confirmed through computational fluid dynamics (CFD) analysis. All the nozzle liners, except the SITVC inserts were made of carbon–phenolic composite. SITVC was provided at four diametrically opposite

locations in the divergent and its capability was demonstrated for the full duration of motor operation in the ground static tests. However, SITVC was used only during the initial 15 s of motor operation. The nozzle throat erosion was approximated based on the measured throat erosion of the same throat material used in similar type of motor. For computation of thrust during motor operation, instantaneous erosion was estimated based on the convective and radiative heat fluxes at the nozzle throat.

Burning rate measurement and burning rate index

Burning rate and pressure index of propellant are important inputs required for performance prediction of any solid motor. The burning rate of the slow-burning propellant used in the HS9 motor was measured utilizing the standard ballistic evaluation motor (BEM) as in the case of other motors/propellants also. The BEM is a small motor of 1 m length and 200 mm diameter, having a star-ported propellant grain. The burning rate was measured as the ratio of the propellant web thickness at the valley of the star to the burn time obtained from the pressure history of the motor during firing. This provides the burning rate at the average pressure of the motor. The pressure index of burning rate (the value of n in the burning rate law, $r = ap^n$) was obtained by testing the BEM at different pressures. The BEM can be tested at different pressures by appropriately selecting different nozzle throat diameters for the motor. In Figure 7, the burning rates measured for the propellant at various pressures are shown. The pressure index thus measured was 0.3. Later, it was decided to obtain the pressure index for this motor for a wide range of pressure values; however, measurement in the standard BEM failed because the motor could not be fired at low pressures (resulted in L^* instability)[5], and there were ignition difficulties as well. The strand burner (acoustic emission) method also did not work since the propellant showed non-ignitability at low pressures in the test chamber of the strand burner[6]. This

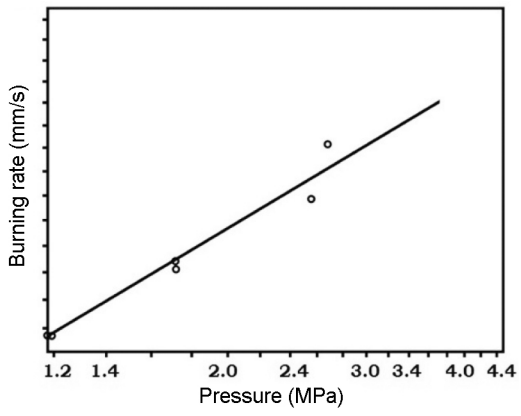

Figure 7. Variation of burning rate of the slow-burning propellants measured by ballistic evaluation motor (BEM).

raised concern on the stable burning of the propellant at low pressures. Hence detailed measurements were done in a newly developed burning rate measurement set-up working on ultrasonic technique[7]. Figure 8 provides the test results and pressure index estimated by this technique. For the motor performance prediction, the burning rate obtained from ultrasonic techniques was used as input ($n = 0.37$). It was observed that the propellant burned smoothly without any burning instability at low pressures and that the pressure indices were different at different pressure values. Later, these pressure indexes were used for performance prediction of the motor. In addition, the burning rate was measured for the HS9 motor propellants using the ultrasonic technique and performance was verified with that predicted using BEM-measured burning rates.

Performance prediction methodology

For large solid boosters, prediction of internal ballistics with sufficient accuracy is important to minimize the number of static tests. Such an accurate prediction is essential for optimizing the motor hardware, such as motor case, insulation, nozzle, and propellant grain at the design stage itself. Alterations of these hardware, after the realization of the motor are expensive and time-consuming. For performance prediction, various influencing parameters (such as erosive burning, nozzle throat erosion, mid-web anomaly, and burning rate augmentation factor) are to be considered. Ballistic performance prediction of the motor is carried out in two steps[8,9]: (1) the motor chamber pressure history estimation by considering nozzle throat erosion rate, and (2) the thrust history estimation which uses predicted pressure history and various flow losses in the nozzle. Computation of pressure and thrust histories involves simultaneous solving of conservation of mass, momentum, energy, perfect gas equation and propellant burning rate law equations. The major influencing parameters required for performance prediction are: (1) propellant grain surface evolution with respect to web thickness; (2) propellant burning rate which is assumed to follow an exponential law $r = ap^n$ with pressure, where a and n are constants derived from laboratory or sub-scale tests; (3) variation of propellant burning rate along radial and axial directions (called mid-web anomaly[10] and burning rate augmentation factor), and (4) erosive burning rate factor (η) as a function of cross-flow velocity[11]. Certain correction factors are also used which are derived from ground firing tests of actual motors, such as (1) nozzle throat erosion rate by a semi-empirical equation containing chamber pressure and throat diameter; (2) combustion efficiency factor which indicates how much the actual combustion deviates from the ideal equilibrium conditions (ratio of actual C^* to the theoretically calculated value[12]), and (3) nozzle efficiency factor which

accounts all the nozzle flow losses. The incremental pressure analysis was adopted for computation of internal ballistics for this motor through division of whole grain into several elements (Figure 9). Performance of the motor was computed considering individual mix burning rate as well as segment average burning rate for comparison. Figure 10 depicts the computation procedure. As the estimation of combustion efficiency is not straightforward, the efficiency factor estimated from other similar motor tests (~0.99) was assumed for the first static test motor and this value was modified to ~0.985 after post-test performance analysis. The burning rate of propellant in an actual large motor is generally different from that measured by ballistic evaluation motors or laboratory tests. Hence, a correction factor on burning rate is always necessary and this factor varies with the type of motor used. Further, the burning rate correction factor is different for different segments and varies along the length of the motor (called augmentation factor) and along the web (called mid-web anomaly factor). It is observed that the scale factor for star port grain is lower than that for cylindrical grain. An average augmentation factor (α) derived from ground firing tests was used for prediction of flight motor. The augmentation factor varied from 6% to 11% along the length of the motor for cylindrical port grains, whereas for the nozzle-end segment (star port) it was close to 0%. For obtaining point-to-point match of the measured performance, burning rate needs to be varied along the radial direction of the web, in addition to axial direction. This scale factor termed as mid-web anomaly (β), is related with the rheology of the propellant mix and casting procedure. Hence, it is difficult to predetermine its value accurately. In the present analysis, the average mid-web anomaly pattern of a similar type of motor was used initially and was later updated based on the first static test. Figure 11 shows the mid-web anomaly pattern for the HS9 motor. Considering these three factors, viz. mid-web anomaly, erosive burning and burning rate augmentation factor, the burning rate equation is modified as

$$r = ap^n(1 + \alpha)(1 + \beta)(1 + \eta). \quad (1)$$

The nozzle throat erosion rates measured in the first and second static tests were 0.009 and 0.01 mm/s respectively.

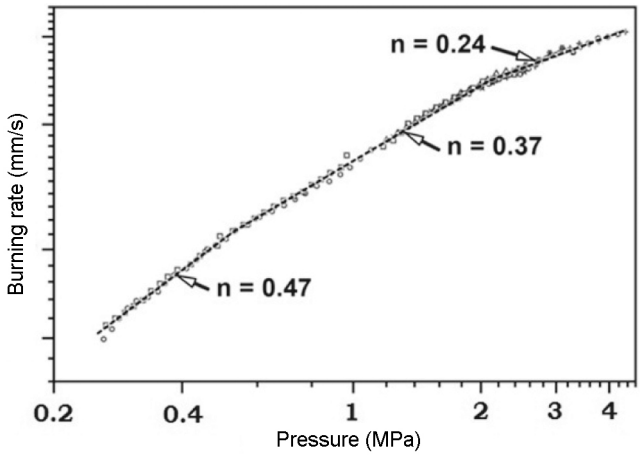

Figure 8. Variation of burning rate of the slow burning propellants measured ultrasonic technique.

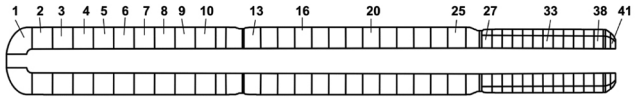

Figure 9. Sections considered for the HS9 motor propellant grain for incremental pressure analysis[20].

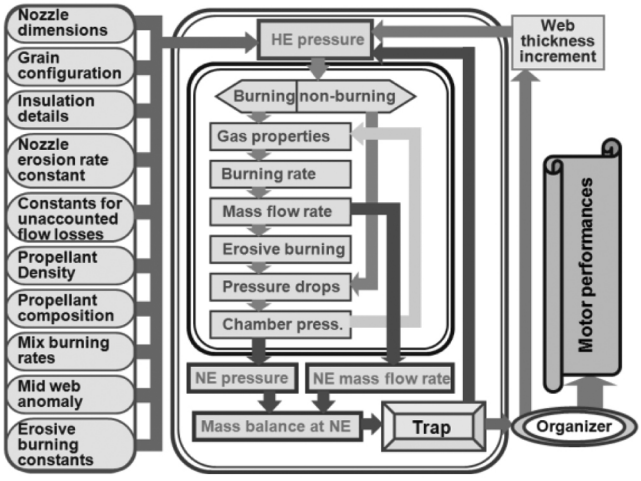

Figure 10. Computation procedure of pressure history prediction.

Hardware design

The motor case has to be a light-weight structure and should withstand the specified internal pressure and mechanical loads such as thrust, inertia, loads due to control system, wind loads and aerodynamic loads during flight. The critical load that is controlling the motor case design is the maximum expected operating pressure (MEOP) of the motor. The motor hardware is to be subjected to acceptance testing called proof pressure test prior to clearing it for propellant processing. The design of the interfaces is critical, since leak tightness of the joint during the motor operating time is essential. Design of the motor and nozzle hardware is carried out based on the elastic–plastic approach as this material is not fracture-prone. Materials selected for motor case and fastener are 15CDV6 (Cr–Mo–V heat treatable steel) and the 35NCD16 (Ni–Cr–Mo) respectively. Motor case shell, head-end dome, and nozzle-end dome are designed for the proof pressure condition. Nozzle hardware design is based on the requirement of stiffness to take care of bonding of ablative liners. Here, strength criteria are

limited to ensure the structural capability to withstand varying pressure and SITVC load. Flanges are designed based on the ultimate pressure condition. Table 4 gives the specification and load factors for the motor. The cylindrical shell thickness of the motor case was arrived at based on membrane shell theory[13], considering the weld mismatch effects. The minimum thickness based on yield was 1.90 mm and the required thickness chosen was 2 mm, considering scaling in heat treatment. Detailed structural analysis was carried out for capturing the stress distribution at various locations. The thickness of the conical shell and cylindrical throat housing was 2.5 mm. The divergent shell thickness was 3 mm. The domes were designed for the proof pressure condition. The head-end dome *Y*-ring and head-end igniter boss were realized from single integral forging. The head-end dome configuration was ellipsoidal, with dome thickness of 2 mm. A reinforcement of 10 mm was provided at the flange-to-dome region to take care of the shock loads. The nozzle-end flange, dome and *Y*-ring were realized from single integral forging. The dome configuration chosen was tori-spherical, with the dome thickness of 3 mm considering bending effects.

Table 4. Specification and load factors of the HS9 motor for hardware design

Motor diameter	1000 mm
L/*D* ratio	11
MEOP	2.6 MPa
Maximum thrust on head-end skirt	370 kN
Maximum allowable weld mismatches	0.15 mm (on long seam) 0.3 mm (on cirumferential seam)
Factor of safety on yield	1.1
Factor of safety on ultimate	1.25

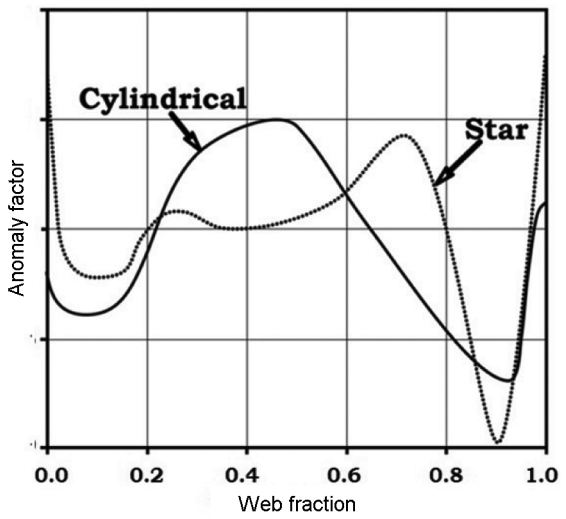

Figure 11. Pattern of mid-web anomaly used for performance prediction of the HS9 motor.

Flange design was carried out using Schneider's approach for design of flat-face flanges with metal-to-metal contact beyond bolt circle[14].

Finite element analysis

Finite element software was used to determine the stresses and deformations[15]. The three-dimensional structural analysis was aimed at predicting the fastener stresses in various flanged joints, viz. igniter boss to head-end dome end closure, motor to nozzle joint. The geometry was modelled using eight-noded brick element with three degrees of freedom per node. The bolt was modelled with solid brick elements and the threaded portion, which engages with the tapped hole, was considered as integral with the flange. The three-dimensional analysis of flanged joint was mainly carried out for finding the bolt bending stresses and joint rotation/flange opening and interface stresses. Pre-load in the bolt was simulated using pre-tension element in finite element software. A friction factor of 0.2 was considered between the interfaces. The analysis was carried out in two load steps. The first load step includes the pre-stressing of the bolt to 60% of the yield strength of the bolt material. The second load step is the combination of pre-stress and internal pressure of 2.9 MPa. Geometric and contact nonlinearity was considered in the analysis. Axial opening at face *O*-ring location in the head-end flange interface was 0.21 mm. Figure 12 shows the 3D finite element model of head-end to motor interface. Axial opening at face *O*-ring location in the motor to nozzle joint was 0.04 mm. Finite element analysis results showed that the maximum stresses were within allowable limits and the minimum margin observed was 0.09 at shell-to-shell long seam weld location.

Figure 13 shows the 3D finite element model of nozzle divergent with SITVC bracket. The four numbers of three-pintle electromechanical injection valves 90° apart were used for SITVC Segment joint: The tongue ring and groove ring with 72 number of pins having 12 mm diameter and two *O*-rings were used for the effective sealing of the joint (Figure 14). Both the rings were designed considering the bearing and tearing strength for the internal pressure load. Analysis showed that the maximum effective stress was at tongue-ring-shell location.

Weld pad: These are small metallic pads welded on the cylindrical shell or nozzle hardware for various purposes, including mounting of cowling for wire tunnel, destruct system, or for attaching bracket to mount other subsystems such as SITVC tanks (Figure 15). Since these weld pads alter the local stiffness and thereby the load path, the stresses on motor and nozzle hardware in the vicinity of these pads can be changed. Hence local, three-dimensional analyses were performed to evaluate the

extent of augmentation in stress due to these weld pads and to assess its criticality. Figure 16 shows the displacement contour of motor case with weld pad. The hydraulic fluid circulation to the fin control actuators of the booster is through two stainless-steel tubes (Figure 17). These tubes are routed along the clamping system placed over the welded pads on the motor. A cowling assembly protects this assembly from aerodynamic effects in flight. The entire assembly has to be structurally integrated to the motor to take care of the various loads occurring during the ascent phase. Integrated structural analysis of hydraulic assembly was carried out to study structural integrity under the critical loading conditions[16].

Proof pressure test

The design of the above systems was demonstrated through the proof pressure test using water as the pressurizing medium. The measured strains were in good agreement with the predicted strains in most of the locations. Based on elasto-plastic approach, the principal and effective stresses have been calculated from measured principal strains. Maximum strain of 3712 μs was measured in hoop direction on the cylindrical shell near the weld pad location. The effective stress at this location was 714 MPa from the measured strains. Margin of safety over 0.2% proof stress of the material was 0.16.

Thermal design

The RLV solid booster motor employs a variety of thermal elements in the form of motor case insulation, nozzle thermal protection liners, segment inhibition, etc. The design of these elements was arrived at based on standard guidelines for launch vehicles. The work-horse materials like ROCASIN (nitrile rubber-based formulation with silica filler), carbon phenolic and IR-1 resin were chosen for case insulation, nozzle liners and segment inhibition respectively. Major design challenges were larger exposure of combustion products on case insulation for the nozzle-end segment, higher grain stand-off distance of

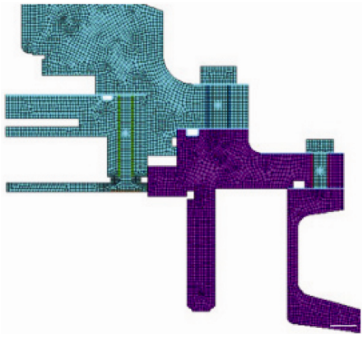

Figure 12. 3D finite element model of head-end to igniter interface.

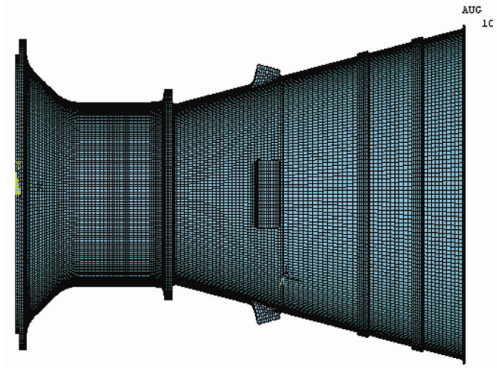

Figure 13. 3D finite element model of nozzle divergent with SITVC bracket.

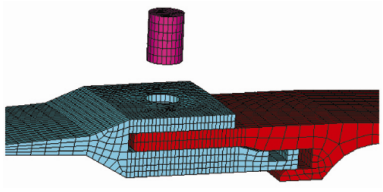

Figure 14. 3D cyclic (one pitch) finite element model of Tang and Clevis segment joint.

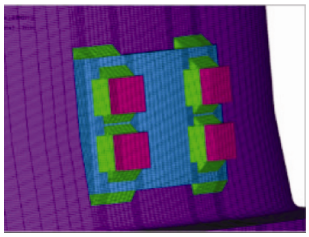

Figure 15. 3D finite element model of weld pads in the nozzle convergent for mounting SITVC tanks.

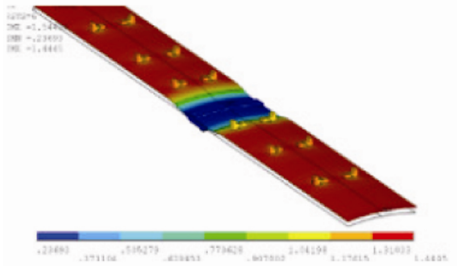

Figure 16. Displacement contour of motor case with weld pad.

Figure 17. Hydraulic tube mounted over the weld pad.

grain from nozzle throat, etc. Thermal management of head-end mounted safe arm (HMSA) for the igniter was challenging, as metallic elements of HMSA are directly exposed to combustion products. The heat fluxes prevalent in the different domains were estimated using boundary layer solutions. Thermo-physical properties of materials were taken from in-house tested properties data book. Computations were based on the two-dimensional char-ablation model[17]. Erosion in convergent and throat liner was governed by two distinctive mechanisms: erosion due to convective heat transfer and erosion due to impingement of alumina particles on the convergent and throat liner. The thermal erosion due to convective heat flux was predicted by nonlinear charring ablative model and erosion due to impingement at the convergent and throat insert was computed using empirical correlations[18], which correlate impingement erosion to velocity of gases and angle of impingement.

Igniter design

The HS9 motor employs a pyrogen igniter (Figure 18). The initiation of the igniter is achieved through HMSA, which can be directly mounted on the igniter-motor head-end dome. Design of the igniter includes ballistic parameters such as ignition delay, initial mass flow rate, average/initial pressure and burn time of the igniter. The pyrogen igniter utilizes a fast burning rate HTPB-AP propellant with an eight-lobe star grain configuration having flame temperature in the range of 2400 K. The igniter grain size is approximately 1000 mm long and 100 mm diameter, and initiation of the grain is achieved by boron–potassium nitrate (B-KNO_3) pelleted pyrotechnics. The case of the igniter is made of glass fibre reinforced plastic (GFRP), which can withstand a maximum operating pressure (MEOP) of 7.5 MPa. The igniter has five canted nozzles at the aft-end which direct the igniter jet at an angle to the propellant surface. Based on the HS9 motor ballistic properties as shown in Figure 19, the igniter parameters originally chosen are given in Table 5; this igniter was used in the first static test (ST-01) of the HS9 motor. Even though the performance of this igniter was normal, a higher ignition delay of the motor was observed, which led to the burnout of the igniter before pressure built up fully in the motor (Figure 20). This indicates the requirement of higher ignition energy to the slow-burning propellant compared to other normal HTPB-AP propellants used in similar types of motors. Based on these observations, the igniter was redesigned to reduce the ignition delay and increase the duration of igniter–motor overlap during the transient phase. The nozzle throat

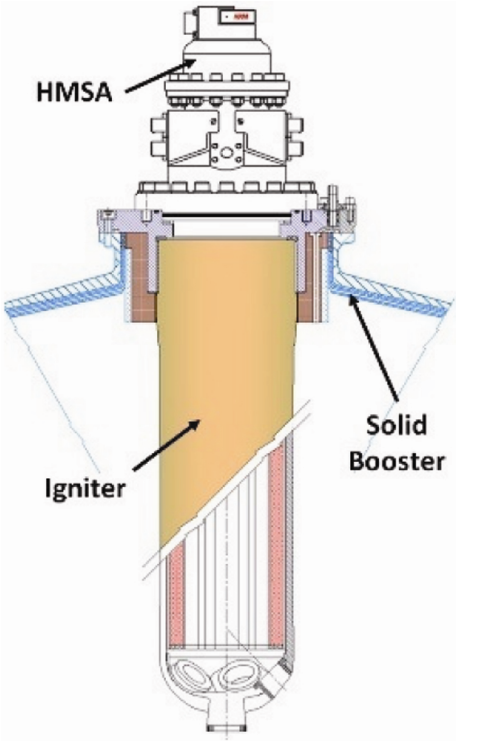

Figure 18. HS9 pyrogen igniter.

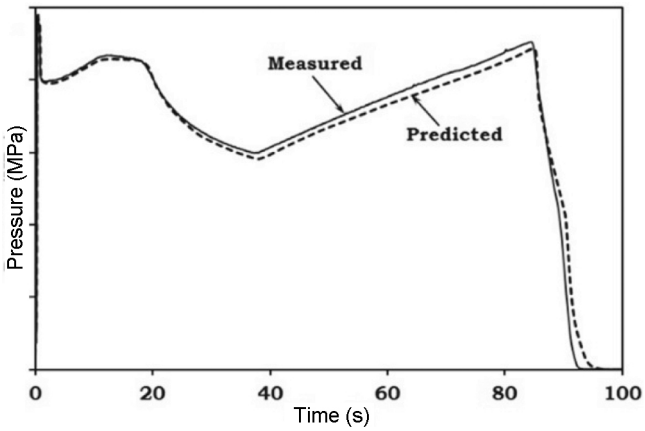

Figure 19. Measured pressure history of the HS9 motor in flight with nominal prediction.

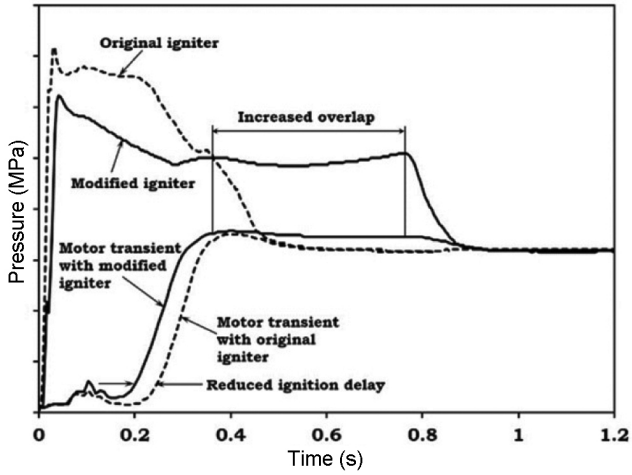

Figure 20. Motor and igniter pressure history during ignition transient phase.

Table 5. Comparison of major igniter parameters

Parameter	Original	Modified
Initial mass flow rate (kg/s)	7.0	10.0
Average pressure (MPa)	4.9	5.0
Burn time (ms)	320	700
Grain configuration	8 lobe star	8 lobe star
Mass discharge coefficient, C_{MD} (kg/m^2 s)	81	128
Average heat flux delivered (J/m^2 s)	4.6×10^6	5.2×10^6

Table 6. Comparison of ballistic parameters measured in the flight motor with the predicted values

Parameter	Predicted	Measured in flight	Allowable deviation
Burn time, s	85.3	84.7	4.6
Action time, s	92.5	91.2	5.0
Maximum pressure (MPa)	2.22	2.27	0.15

diameter was obtained considering choked flow conditions. The mass flow rate was determined by the burning surface area of the igniter grain and burning rate of the propellant. The average heat flux of the igniter was computed using the following empirical equation[19]

$$H_f = 6.442 Q_{ig} (m_{ig}/A_p)^{0.8}, \quad (2)$$

where H_f is the heat flux, Q_{ig} the igniter propellant energy (cal/g), m_{ig} the igniter mass flow rate (kg/s) and A_p is the motor port cross-sectional area (cm^2). A higher mass flow rate of the igniter produces early ignition by increasing the heat flux from the igniter, which has also been confirmed by earlier studies[20]. In the modified igniter, initial mass flow rate was increased by about 20% of the original design by providing additional propellant burning surface (by increasing port diameter as well as length).

Adequate overlap over the motor ignition period was achieved by increasing the web thickness of the igniter grain by 5 mm. The modified igniter was successfully qualified in the second static test of the HS9 motor (ST-02), wherein ignition delay of the motor was reduced by 80 ms and adequate overlap (about 400 ms) of igniter burn time over motor transient phase was achieved.

Head-end mounted safe arm: Ignition safe-arm devices are necessary to prevent inadvertent functioning of a rocket motor due to accidental triggering, or due to stray currents induced by radio frequency disturbances, electromagnetic interference or static electricity. Existing solid motors of ISRO use a remote mounted electromechanical safe-arm device in combination with pyro-circuit elements. The total assembly occupies considerable space on the head-end dome of the motor. In the case of the present RLV programme, space constraint was there on the head-end dome due to positioning of various avionics packages and flight batteries. This led to the design and development of HMSA, which is directly mounted over the igniter head-end (Figure 18). In addition, this design has the advantages of reduced system complexity, simplified launch pad operations and increased reliability by markedly reducing the number of explosive interfaces.

Static tests of the motor

The first static test of the motor (ST-01) was successfully conducted on 19 November 2008. This test showed some difference from the prediction mainly because of very low nozzle throat erosion in the test than expected (one order less compared to the prediction). The low nozzle throat erosion can be either due to the use of burning rate retardant in the propellant which reduces the adiabatic flame temperature of the combustion products, or due to the fast completion of nozzle-end grain (which has a star configuration, whereas other segments have cylindrical port configuration), resulting in a larger stand-off distance of the propellant grain from the nozzle[5]. In Figure 4, the measured thrust history is compared with that predicted. The mission analysis based on the delivered thrust history of the first static tested motor showed higher dynamic pressure on the vehicle during the transonic phase. This was corrected through minimal changes by reducing the outer diameter of the nozzle-end grain and correspondingly increasing the insulation thickness (Figure 5). This resulted in early consumption of the nozzle-end grain and early thrust fall which reduced the dynamic pressure on the vehicle to the acceptable limit. In fact, this correction process increased the inert mass, decreased the propellant mass, and thereby decreased the total impulse. However, the correction was adopted because the dynamic pressure reduction was essential for the mission. The second static test (ST-02) was carried out with this modification, and the predicted performance was close to the measured performance (Figure 6). All the ballistic parameters and subsystem performances were validated in ST-01 static test; minor modification in NS grain geometry was as expected. The close match of ballistic parameters gave the confidence for further processing of the flight motor.

Performance of the motor in flight

The measured ballistic parameters in connection with the HS9 motor were the motor and igniter pressure values. All the data were transmitted to the ground in 12 bit resolution with 2 ms period. The transducer accuracy for the pressure data is ±0.02 MPa. In addition to the pressure data, the vehicle acceleration data were also available which provide information on the thrust generated by the vehicle.

Ballistic performance of the motor

In Figure 19, the measured pressure history of the motor is compared with the pre-flight prediction. It shows that the measured pressure history closely matches with prediction, but a small mismatch is seen towards the end

of burning of the motor and at the tail-off. Maximum deviation in the equilibrium burning region is 0.06 MPa at the burn time of the motor. Table 6 compares various ballistic parameters measured in the motor with those predicted. It shows that all the measured parameters are close to those predicted and are well within the mission limits. However, deviation in the measured pressure integral is marginally higher (by 0.1 MPa.s) compared to that expected. This can be due to two reasons: (1) the telemetry pressure data can be slightly biased towards the upper side due to the transducer accuracy, calibration and data transmission errors, or (2) lower nozzle throat erosion rate than that expected. A bias error of 0.02 MPa in the pressure channel is sufficient for observed deviation in the pressure integral and accuracy limit of the transducer alone falls in this range. The second reason of lower throat erosion also cannot be ruled out because the throat erosion was actually measured in the motor when static tested was one order of magnitude less than that measured in other 1000 mm diameter booster motors with the same carbon phenolic throat material. The assumed throat erosion is less than 1 mm for the prediction and the pressure integral measured indicates that the erosion can be further low (close to zero).

Figure 20 shows the pressure recorded in the igniter and the motor. It shows that the igniter performed as expected and good overlap is obtained by the igniter action time over motor pressure rise time.

Conclusion

A solid motor of 1 m was designed and successfully used for the launch of RLV-TD. The motor met all the specific requirements for the flight. The grain of the motor was designed such that the motor burns for ~90 s and produces an average thrust of 250 kN. A deep slotted grain configuration was chosen for the nozzle end in order to reduce the erosive burning, and necessary correction was made on this grain in order to limit the dynamic pressure below the acceptable limit. A slow-burning propellant with oxamide as the burning rate retardant was developed and qualified through two ground-firing motor tests. The case of the motor was designed with 15CDV6 metal and nozzle throat was carbon-phenolic. The igniter was pyrogen-type, which met the requirement of sufficient overlap of the igniter action over pressure build-up in the motor to ensure ignition. In addition, the critical technology related to HMSA was successfully demonstrated using this motor. The achieved ballistic performance of the motor in RLV flight was close to the pre-flight prediction, and all the performance parameters were well within the mission limits.

1. Sutton, G. P., *Rocket Propulsion Elements*, Wiley, New York, USA, 1992, 6th edn.
2. Keswani, S. T., Andiroglu, E., Campbell, J. D. and Kuo, K. K., Recession behaviuor of graphitic nozzles in simulated rocket motors. *J. Spacecraft Rockets*, 1985, **22**(4), 396–397.
3. Kalt, S. and Badal, D. L. Conical rocket nozzle performance under flow separated conditions. *J. Spacecraft*, 1965, **2**(3), 447–449.
4. Price, E. W., L* instability, non-steady burning and combustion instability of solid propellant. *J. Am. Inst. Aeronaut. Astronaut.*, 1992, 325–361.
5. Saber, A. J., Johnston, M. D., Caveny, L. H., Summerfield, M. and Koury, J. L., Acoustic emissions from burning propellant strands. In Proceedings of the 11th JANNAF Combustion Conference, CPIA Publication No. 261, Laurel, MD, USA, December 1974, vol. 1, pp. 409–427.
6. Jeenu, R., Kiran, P. and Deepak, D., Industrial adaptation of ultrasonic technique of propellant burning rate measurement using specimens. *J. Propul. Power*, 2013, **29**(1), 216–226.
7. Miller, W. H. and Barrington, D. K., A review of contemporary solid rocket motor performance prediction techniques. *J. Spacecraft Rockets*, 1970, **7**(3), 225–237; doi:10.2514/3.29911.
8. Jeenu, R., Jayaprakash, J., Prasanth, C., Srinivasan, V. and Narayanamoorthy, N., Performance prediction for the first static test of a large solid booster motor, IAC-10-C4.2.2, 2010.
9. Heister, S. D., Ballistics of solid rocket motors with spatial burning rate variations. *J. Propul. Power*, 1993, **9**(4), 649–651.
10. Mukunda H. S. and Paul, P. J., Universal behaviour in erosive burning of solid propellants. *Combust. Flame*, 1997, **109**, 224–236.
11. Gordon, S. and McBride, B. J., Computer program for calculation of complex chemical equilibrium compositions and applications. NASA Reference Publication 1311, Ohio 44135, October 1994.
12. John F. Harvey, *Theory and Design of Pressure Vessels*, ISBN:0-442-23248-9, New York.
13. Schneider, R. W., Flat face flanges with metal to metal contact beyond the bolt circle. *J. Eng. Power, Trans. ASME*, 1968, vol. 1, 82–88.
14. ANSYS Basic Analysis guide Section 2.9 'Defining the pretension in a joint fastener' and Section 14.179 'PRETS179-Pretension', Canonsburg, November 2004.
15. Paul Murugan, J. and Kurian, T., Design approach adopted for ensuring the structural integrity of a hydraulic line assembly along the SRM for a RLV-TD mission. In 66th IAC, Jerusalem, Israel, 2015.
16. Quan, V., Quasi-steady solution for ablation–erosion heat transfer. *J. Spacecraft Rockets*, 1970, **7**(3), 355–357.
17. Ketner, D. M. and Hess, K. S., Particle impingement erosion. In AIAA 15th Joint Propulsion Conference, Utah, 18–20 June 1979.
18. Space Vehicle Design Criteria (Chemical Propulsion)-Solid Rocket Motor Igniters, NASA SP-8051.
19. Moore, J. D., Flame spreading phenomena in a head end fin-slot segment of a subscale motor simulating the space shuttle boosters. Ph D thesis, Department of Mechanical and Nuclear Engineering, Pennsylvania State University, May 2008.
20. Jeenu, R., Prasanth, C., Jayaprakash, J., Abraham, P. J., Srinivasan, V. and Ramakrishnan, S., Strategies of the grain configuration design for large solid booster motors. In IAC-12, C4, 2, 4, x13449. 63rd International Astronautical Congress, Naples, Italy, 1–5 October 2012.

ACKNOWLEDGEMENTS. We thank all the concerned developmental agencies in the Indian Space Research Organization for their invaluable inputs provided directly or indirectly. We also thank Dr R. Jeenu (VSSC, Thiruvananthapuram) for compilation and editing of this manuscript.

doi: 10.18520/cs/v114/i01/74-83